

An experimental study of the unsteady vortex structures in the wake of a root-fixed flapping wing

Hui Hu · Lucas Clemons · Hirofumi Igarashi

Received: 7 October 2010/Revised: 25 January 2011/Accepted: 1 February 2011/Published online: 19 February 2011
© Springer-Verlag 2011

Abstract An experimental study was conducted to characterize the evolution of the unsteady vortex structures in the wake of a root-fixed flapping wing with the wing size, stroke amplitude, and flapping frequency within the range of insect characteristics for the development of novel insect-sized nano-air-vehicles (NAVs). The experiments were conducted in a low-speed wing tunnel with a miniaturized piezoelectric wing (i.e., chord length, $C = 12.7$ mm) flapping at a frequency of 60 Hz (i.e., $f = 60$ Hz). The non-dimensional parameters of the flapping wing are chord Reynolds number of $Re = 1,200$, reduced frequency of $k = 3.5$, and non-dimensional flapping amplitude at wingtip $h = A/C = 1.35$. The corresponding Strouhal number (Str) is 0.33, which is well within the optimal range of $0.2 < Str < 0.4$ used by flying insects and birds and swimming fishes for locomotion. A digital particle image velocimetry (PIV) system was used to achieve phased-locked and time-averaged flow field measurements to quantify the transient behavior of the wake vortices in relation to the positions of the flapping wing during the upstroke and down stroke flapping cycles. The characteristics of the wake vortex structures in the chordwise cross planes at different wingspan locations were compared quantitatively to elucidate underlying physics for a better understanding of the unsteady aerodynamics of flapping flight and to explore/optimize design paradigms for the development of novel insect-sized, flapping-wing-based NAVs.

List of symbols

A	Flapping amplitude
b	Span of the flapping frequency
C	Chord length of the flapping wing
f	Flapping frequency
h	Non-dimensional flapping amplitude, $h = A/C$
k	Reduced frequency, $k = 2\pi f C / U_\infty$
Str	Strouhal number, $Str = f A / U_\infty$
U_∞	Forward flying speed or incoming flow velocity
U, V	Mean flow velocity
u, v	Instantaneous flow velocity
x, y, z	Cartesian coordinate system
ω_z	Spanwise vorticity

1 Introduction

With the rapid progress made in micro-electromechanical system (MEMS), micro fabrication, miniaturized power cells, remote communication, imaging and control devices, and other enabling technologies, a new class of miniaturized aircraft known as nano-air-vehicles (NAVs) is becoming possible in the not so distant future. According to the definition given by Defense Advanced Research Projects Agency (DARPA), NAVs refer to “airborne vehicles no larger than 7.5 cm in length, width or height, capable of performing a useful military mission at an affordable cost and gross takeoff weight of less than or equal to 10 g”. The potential of NAVs opens up new possibilities in the formulation of various civilian and military strategies with respect to information superiority in urban operations. Their main attributes are expected to be low cost, low weight, little to no logistical footprint, mission versatility, endurance, low visibility, covertness, and precision. The

H. Hu (✉) · L. Clemons · H. Igarashi
Department of Aerospace Engineering, Iowa State University,
Ames, IA 50011, USA
e-mail: huhui@iastate.edu

real mission niche for such insect-sized aircraft may well be in the indoor setting where there is currently no reconnaissance asset available for various civilian and military applications.

Aerodynamic design challenges for NAVs are driven by a combination of very low Reynolds number physics and the requirement for a multi-functional platform structure. These challenges have already motivated many novel approaches for NAV designs with fixed-wing, rotary wings, flapping wings, or even designs like maple tree seeds (Wood 2008; Youngren et al. 2008). Fortunately, these challenges are similar to the aerodynamic challenges overcome with micro-air-vehicle (MAVs) (Mueller 2001) and researchers can build upon this knowledge. However, the limited volume of space available within NAVs makes the aerodynamic challenges even greater than those overcome by MAVs. In general, fixed-wing solutions for NAV applications are discounted because they require either relatively high forward speed or large wings. Although rotary wings offer good agility and vertical-take-off-and-landing (VTOL) capability, they suffer from wall-proximity effects, are too noisy, and usually are inefficient for low Reynolds number flight (Bohorquez et al. 2003; Ramasamy et al. 2006). As demonstrated by flying insects and birds, flapping flight is advantageous for its superior maneuverability and lifting capability at low Reynolds numbers.

Flapping-wing systems as inspired by bird and insect flight generally involve the wing completing pitching, plunging, and sweeping components of motion over a flapping cycle (Maxworthy 1981; Sunada and Ellington 2001; Dickinson et al. 1999). Different mechanisms such as pneumatic and motor-driven actuators with gear systems have been widely used to generate complex flapping motions. However, those mechanisms often suffer from heavy weight and complexity, which limit the flapping frequency of the mechanical flapping mechanisms (i.e., usually less than 15 Hz). Piezoelectric materials are widely used in smart structures such as sensors and actuators due to their high output force, compact size, and high power density (Niezrecki et al. 2001). The concept of piezoelectric fans, which couple piezoelectric unimorph/bimorph to attached flexible blades and can flap at a frequency of 60–200 Hz, was originally suggested as a compact, low power, noiseless cooling technology for the effective cooling of electronic devices such as laptop computers and DVD players (Toda 1981; Yoo et al. 2000; Wu et al. 2003). Several studies have also been conducted in recent years to leverage the unique feature of piezoelectric fans to explore their potential applications as the compact flapping wings for NAV/MAV designs (Cox et al. 2002; Park et al. 2004, and Chung et al. 2009). More recently, the tethered-takeoff of a piezo-based, insect-sized flapping-wing NAV has been

demonstrated successfully (Wood 2008). It should be noted that to author's best knowledge, no study has ever been conducted so far to investigate the aerodynamic aspects of compact, root-fixed, piezoelectric flapping wings with the wing size, stroke amplitude, and flapping frequency within the range of insect characteristics. In the present study, an experimental investigation was conducted to quantify the unsteady aerodynamic characteristics of a root-fixed piezoelectric flapping wing with the wing size, stroke amplitude, and flapping frequency within the range of insect characteristics for the development of novel insect-sized NAVs.

It is well known that flapping airfoils/wings generate thrust at certain combinations of flapping frequency and amplitude. While numerous investigations on flapping airfoils/wings were concentrated on pure pitching or combined plunging and pitching motions, many studies have also been conducted on pure plunging motion. Garrick (1936) determined the propulsive efficiency of a plunging and pitching flat-plate airfoil as a function of the flapping frequency, with the assumption of potential flow and small-amplitude oscillation. Freymuth (1988), Jones et al. (1996), Lai and Platzer (1999) show that the wakes of 2-D plunging airfoils can be characterized as drag-producing, neutral, or thrust-producing depending on the plunge frequency and amplitude. As shown in Fig. 1, drag-producing wakes are found to have velocity profiles that show a momentum deficit when time averaged, typically with von Karman vortex street wake configurations with two alternating vortex rows, clockwise above and anti-clockwise below for a flow from left to right. Vortex pairs form mushroom-like structures that are tilted upstream. Thrust-producing wakes show a momentum surfeit, or jet, superimposed on the momentum-deficit velocity profile in the time-averaged flow, such that the thrust of the jet is greater than the inherent drag of the airfoil. The wake configuration is typically a reverse von Karman vortex street with two rows of alternating vortices with anti-clockwise above and clockwise below, so that vortex pairs form downstream tilted mushrooms. Neutral wakes, where the thrust due to plunging balances the inherent drag, may show multiple vortex shedding per half-cycle, and vortex pairs are not tilted.

While useful information has already been uncovered through those previous studies, much work is still needed for a better understanding of fundamental mechanism of flapping flight for optimum aerodynamic design of NAVs/MAVs. For example, most of the previous studies about the evolution of the unsteady vortex structures in the wakes of flapping wings/airfoils were carried out by using two-dimensional (2-D) airfoils in flapping motion. Considering more practical configurations used in NAV/MAV designs with root-fixed three-dimensional (3-D) flapping wings, the

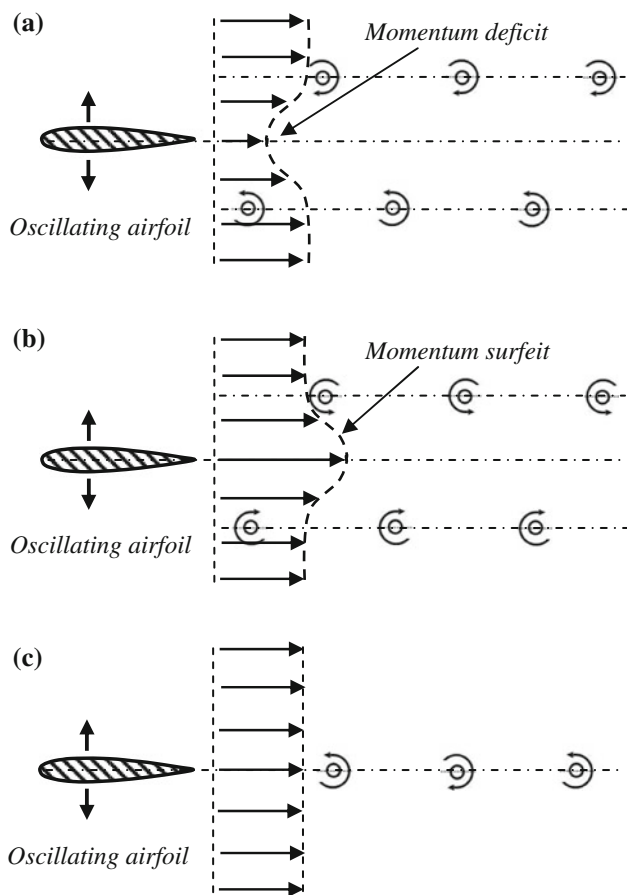


Fig. 1 Three typical wake flow patterns in the downstream of 2-D oscillating airfoils. **a** Drag-producing wake. **b** Thrust-producing wake. **c** Neutral wake

effects of spanwise variations in flapping amplitude and the existence of additional wingtip vortex for a root-fixed flapping wing on the evolution of wake vortex structures as well as the resultant aerodynamic forces (i.e., lift and thrust) have not been fully explored. It should also be noted that while the wingtip displacement observed in the flapping flight of birds and insects was found to be usually on the order of averaged chord length of the wings, the plunging/pitching amplitudes of the flapping airfoils/wings used in most of previous studies were usually quite small, i.e., less than 20% of the airfoil/wing chord length (Frey-muth 1988; Jones et al. 1996; Lai and Platzer 1999; Lewin and Haj-Hariri 2003; Young and Lai 2004; Bohl and Ko-chesfahani 2009). The effects of the much large flapping amplitude (i.e., $h = A/C > 1.0$) on the evolution of the unsteady vortex structures in wakes of root-fixed 3-D flapping wings are still unclear. Since mechanical-based flapping mechanism systems, which often suffer from heavy weight and complexity, were used in previous experimental studies, the flapping frequency of the mechanical-based flapping mechanisms is usually less than 15 Hz, which is much lower than the wing beating

frequency of the small birds and insects which have comparable size as NAVs, e.g., humming birds (40–60 Hz) and dragonflies (30–100 Hz). Besides, the dimension of the flapping airfoil/wing models used in most of the previous experimental studies were significantly larger compared with the size definition of NAVs. With these in mind, we conducted the present study to characterize the aerodynamic performance of a root-fixed 3-D flapping wing with the wing size, stroke amplitude and flapping frequency within the range of insect characteristics. The objective of the present study is to elucidate underlying physics for a better understanding of the unsteady aerodynamics of flapping flight and to explore/optimize design paradigms for the development of novel insect-sized, flapping-wing-based NAVs.

2 Experimental setup

The experimental study was conducted in a closed-circuit low-speed wind tunnel located in the Aerospace Engineering Department of Iowa State University. The tunnel has a 2.5 m long \times 0.30 m wide \times 0.30 m high test section, and the walls of the test section are optically transparent. The tunnel has a 40:1 contraction section upstream of the test section with honeycombs, screen structures and a cooling system installed ahead of the contraction section to provide uniform low turbulent incoming flow into the test section.

Figure 2 shows the schematic of the piezoelectric flapping wing used in the present study. The tested piezoelectric flapping wing has a rectangular planform with a chord length 12.7 mm (i.e., $C = 12.7$ mm), wingspan 34 mm (i.e., $b = 34$ mm), and thickness 0.26 mm. A

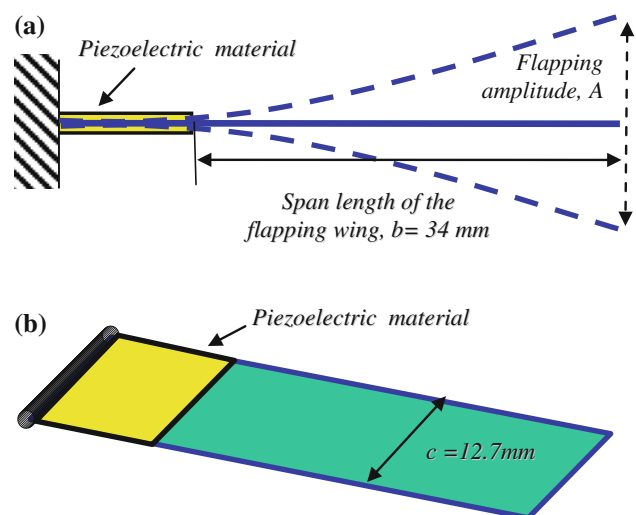
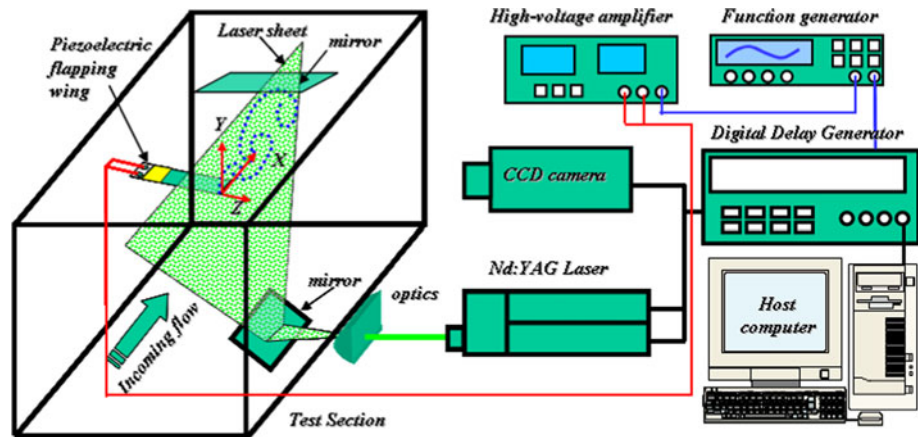


Fig. 2 The schematic of the root-fixed piezoelectric flapping wing used in the present study. **a** Side view. **b** Top view

Fig. 3 Experimental setup for the PIV measurements used in the present study



piezoelectric actuator film (~ 0.1 mm in thickness) was bonded at the root of the tested wing to drive the rectangular wing in flapping motion. In the present study, the velocity of the incoming flow was set as $U_\infty = 1.40$ m/s, which corresponds to a chord Reynolds number of $Re_C = 1,200$. The turbulence intensity of the incoming flow was found to be about 1.0%, measured by using a hot-wire anemometer, with the test model installed in the test section.

Figure 3 shows the experimental setup used in the present study. A small mount unit, which includes a mount plate and two hollowed supporting legs, was designed to fix the root of the test flapping wing in the middle of the wind tunnel test section in order to minimize the effects of wind tunnel walls on the evolution of the vortex and flow structures in the wake of the piezoelectric flapping wing. Two electric wires would go through the hollowed supporting legs of the mount unit to connect to the piezoelectric flapping wing. A sinusoidal AC voltage, which was supplied by using a function generator and amplified through a high-voltage amplifier, was used to drive the piezoelectric flapping wing. The wing would be in plunging motion with the same frequency as the applied AC voltage. The amplitude of the plunging motion was found to reach its peak value when the frequency of the applied AC voltage matches the resonance frequency of the piezoelectric wing, which is 60 Hz for the present study. As shown in Fig. 4, the peak-to-peak flapping amplitude of the wingtip was found to increase linearly with the applied AC voltage. It should also be noted that the piezoelectric flapping wing was found to bend along spanwise direction under dynamic conditions; however, no observable torsional mode of bending (i.e., no flex along chordwise direction) was found in the present study.

As revealed by Koochesfahani (1989), for a given flapping frequency and stroke amplitude, a variety of complex wake vortex structures can be generated by simply changing the shape of the wave-form of the flapping

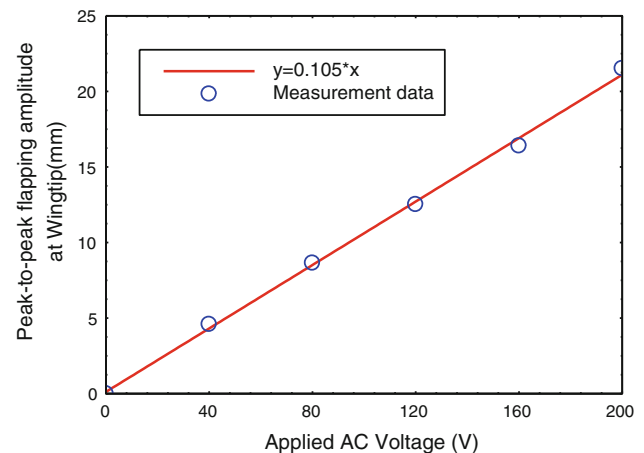


Fig. 4 The profile of the measured flapping amplitude at wingtip as a function of the AC voltage applied to the piezoelectric actuator

motion. An experiment was conducted in the present study to measure the wave-form of the plunging trajectory of the wingtip as the piezoelectric wing was driven by a sinusoidal AC voltage. As shown clearly in Fig. 5, the trajectory of the wingtip was sinusoidal when the piezoelectric flapping wing was driven by a sinusoidal AC voltage.

A dimensionless parameter that is widely used to quantify flapping flight is Strouhal number (Str). In addition, reduced frequency, k , is also widely used to characterize the aerodynamic performance of flapping flight. By using non-dimensional flapping amplitude, h , the relationship between the product of kh and the Strouhal number (Str) can be written as $kh = 2\pi Str$. Extensive previous studies with either pitching or heaving airfoils/wings have revealed that optimum propulsion efficiency for a flapping airfoil/wing (defined as the ratio of aerodynamic/hydrodynamics power output to mechanical power input) would be within the range of $0.2 < Str < 0.4$ (Triantafyllou et al. 1991; Anderson et al. 1998; Read et al. 2003 and Wang 2000). It has also been found that natural selection is likely to tune birds and insects to fly in the range of

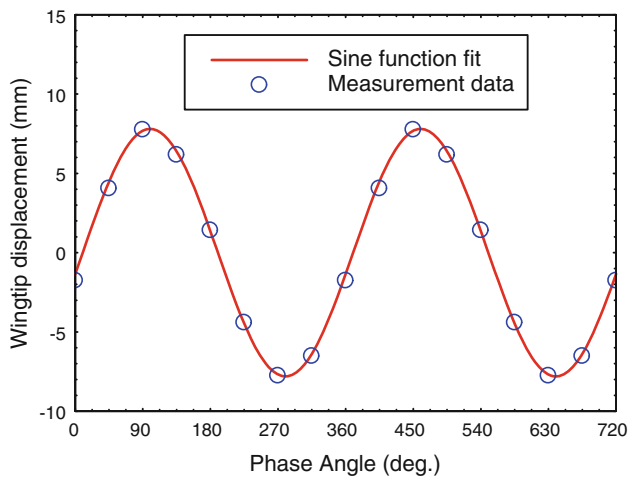


Fig. 5 The profile of the measured wingtip position as a function of the phase angle of tested wing in flapping motion

$0.2 < Str < 0.4$. For example, Taylor et al. (2003) analyzed the flapping frequencies and amplitudes of 42 species of birds, bats, and insects and found that the flying creatures operate within a narrow range of Strouhal number of $0.2 < Str < 0.4$ for optimum propulsion efficiency. Similar results were also found to be true for dolphins, sharks, bony fish, and other swimming fishes using flapping tails/fins for locomotion (Triantafyllou et al. 1993). For the present study, the peak-to-peak flapping amplitude at the wingtip of the root-fixed piezoelectric flapping wing was found to be 15.60 mm (i.e., $A = 15.60$ mm; $h/C = 1.35$). Following the work by Taylor et al. (2003) to use half of the peak-to-peak flapping amplitude at wingtip to calculate the equivalent Strouhal number (Str) for a root-fixed 3-D flapping wing, the equivalent Strouhal number (Str) for the present study was found to be 0.33 (i.e., $Str = 0.33$), which is well within the optimal range of $0.2 < Str < 0.4$ usually used by flying birds and insects as well as swimming fishes.

A digital particle image velocity (PIV) system was used in the present study to make detailed flow field measurements to quantify the evolution of the wake vortex structures in relation to the position of the piezoelectric wing during the upstroke and down stroke cycles. The flow was seeded with 1–5- μ m oil droplets. Illumination was provided by a double-pulsed Nd:YAG laser (NewWave Gemini 200) adjusted on the second harmonic and emitting two pulses of 200 mJ at the wavelength of 532 nm with a repetition rate of 10 Hz. The laser beam was shaped to a sheet by a set of mirrors, spherical, and cylindrical lenses. The thickness of the laser sheet in the measurement region is about 1.0 mm. As shown in Fig. 2, a mirror was installed on the top of the wind tunnel to reflect the illuminating laser sheet back to the measurement region in order to eliminate the shadow region of the piezoelectric flapping wing for PIV measurements. A high-resolution 12-bit

(1,600 \times 1,200 pixel) CCD camera (PCO1600, Cooke-Corp) was used for PIV image acquisition with the axis of the camera perpendicular to the laser sheet. The CCD camera and the double-pulsed Nd:YAG laser were connected to a workstation (host computer) via a Digital Delay Generator (DDG, Berkeley Nucleonics, Model 565), which controlled the timing of the laser illumination and image acquisition.

During the experiments, the sinusoidal signal supplied by the function generator to drive the piezoelectric flapping wing was also used as the input signal to the Digital Delay Generator (DDG) to trigger the PIV system to conduct phase-locked PIV measurements. By adding different time delays between the input sinusoidal signal and the TTL signal output from the DDG to trigger the digital PIV system, phase-locked PIV measurements at different phase angles (i.e., corresponding to different positions of the flapping wing) in the course of the upstroke and down stroke flapping motion for the flapping wing were accomplished. At each pre-selected phase angle, 160 frames of instantaneous PIV measurements were used to calculate phase-averaged flow field around the flapping wing. In addition to phase-locked PIV measurements, time-averaged PIV measurements were also carried out by simply disconnecting the phase-locking between the flapping motion of the flapping wing and the PIV system in order to derive the mean flow field around the flapping wing.

In the present study, instantaneous PIV velocity vectors were obtained from the acquired PIV images by using a frame to frame cross-correlation technique involving successive frames of patterns of particle images in an interrogation window 32×32 pixels. An effective overlap of 50% of the interrogation windows was employed to derive instantaneous velocity vectors for the PIV image processing. After the instantaneous velocity vectors (u_i, v_i) were determined, instantaneous spanwise vorticity (ω_z) could be derived. The time-averaged quantities such as mean velocity (U, V) and ensemble-averaged spanwise vorticity (ω_z) distributions were obtained from a cinema sequence of 500 frames of instantaneous velocity fields in each chordwise cross planes. The uncertainty level for the instantaneous velocity measurements is estimated to be within 2.0% of the local flow velocity and that of the spanwise vorticity data is expected to be within 10.0% of the local vorticity. Further information about the experimental setup, the test piezoelectric flapping wing, and PIV measurements is available in Clemons (2009).

3 Results and discussions

Figures 6, 7, 8 show the phase-locked PIV measurement results in the chordwise cross planes passing 50%

Fig. 6 Phase-locked PIV measurement results in the chordwise cross plane at 50% wingspan. **a** Wing at the upmost position, down stroke starts. **b** Wing at the neutral position, during down stroke. **c** Wing at the bottom most position, up stroke starts. **d** Wing at the neutral position, during upstroke

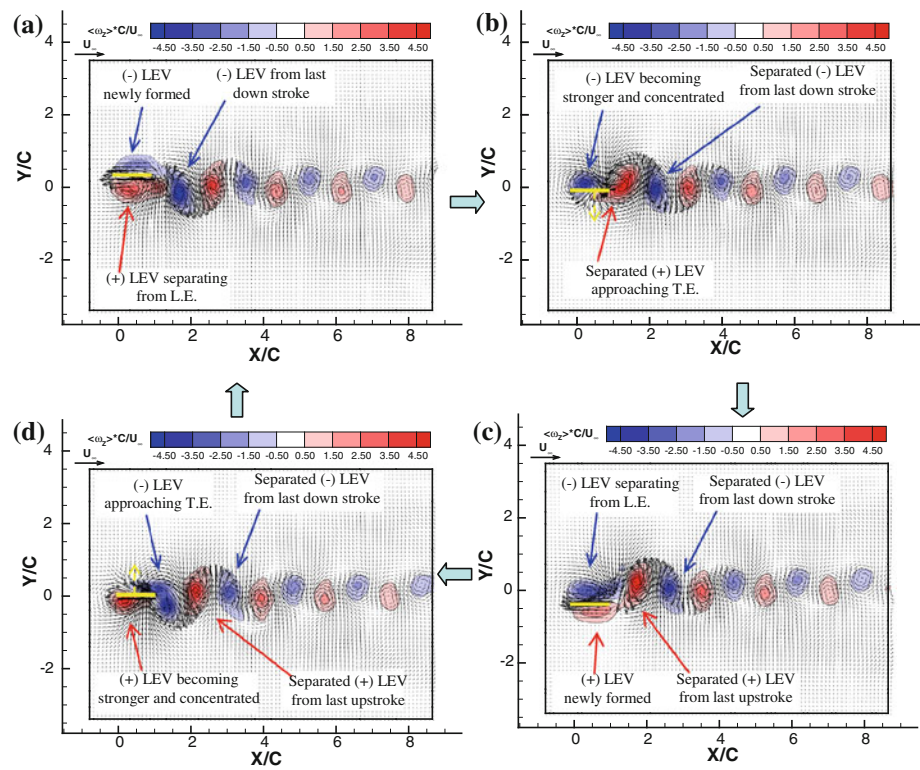
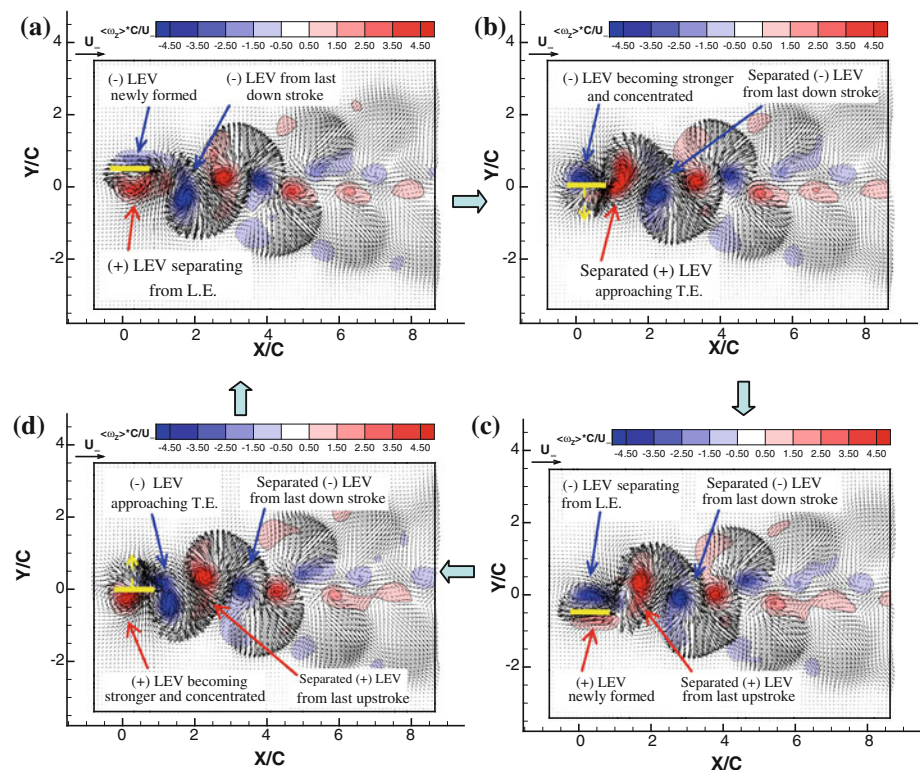


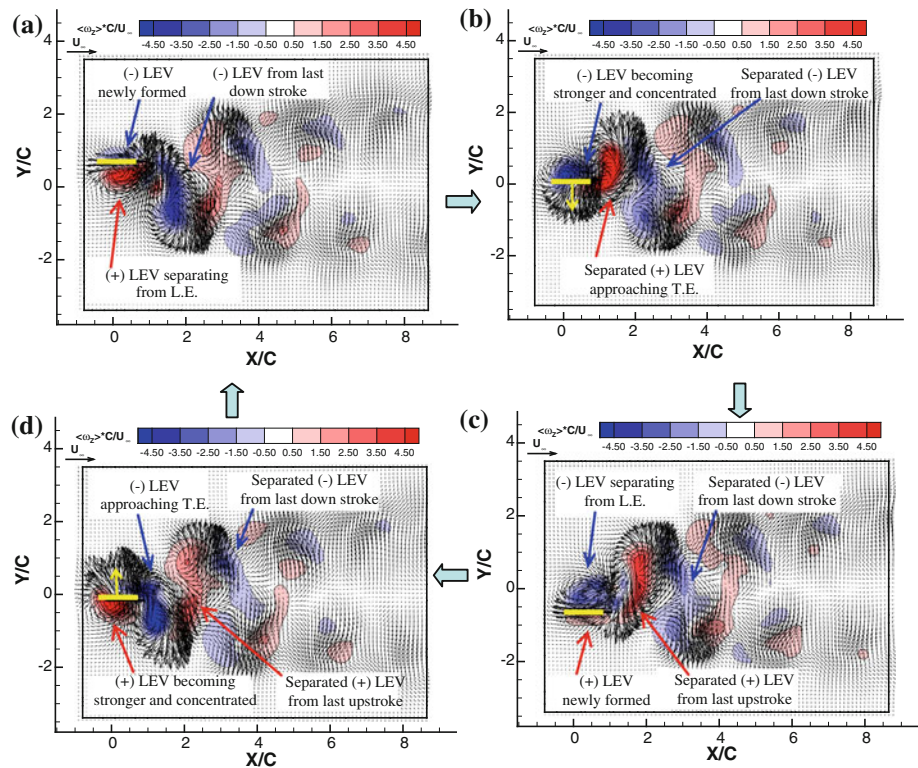
Fig. 7 Phase-locked PIV measurement results in the chordwise cross plane at 75% wingspan. **a** Wing at the upmost position, down stroke starts. **b** Wing at the neutral position, during down stroke. **c** Wing at the bottom most position, up stroke starts. **d** Wing at the neutral position, during upstroke



wingspan, 75% wingspan, and 100% wingspan (i.e., wingtip) of the root-fixed flapping wing, respectively. The static angle of attack (AOA) of the piezoelectric flapping wing was set to be zero (i.e., $AOA = 0$ deg). For the

phase-locked PIV measurements shown in the plots, the positions of the piezoelectric flapping wing were at its upmost position (i.e., at the end of upstrokes or beginning of down strokes), neutral position during down strokes,

Fig. 8 Phase-locked PIV measurement results in the chordwise cross plane at wingtip. **a** Wing at the upmost position, down stroke starts. **b** Wing at the neutral position, during down stroke. **c** Wing at the bottom most position, up stroke starts. **d** Wing at the neutral position, during upstroke



bottom most position (i.e., at the end of down strokes or the beginning of upstrokes), and the neutral position during upstrokes, respectively. In the figures, the uniform incoming velocity U_{∞} was subtracted from the measured flow velocity fields in order to reveal the unsteady vortex structures induced by the flapping motion more clearly.

The phase-locked PIV measurements at different wing-span locations revealed very similar scenarios about the formation and separation process of the leading edge vortex (LEV) structures on the lower and upper surfaces of the flapping wing. As shown clearly in Figs. 6a, 7a, and 8a, when the piezoelectric flapping wing was at its upmost position to start a down stroke, the anti-clockwise (positive) LEV structure on the lower surface of the wing formed during previous upstroke cycle was found to begin to separate from the leading edge (L.E.) of the flapping wing. While the clockwise (negative) LEV generated during previous down stroke would shed from the trailing edge (T.E.) of the flapping wing to form a wake vortex, a new clockwise LEV was found to form on the upper surface of the piezoelectric flapping wing. During the down strokes of the flapping motion, while the clockwise LEV structure newly formed on the upper surface of the flapping wing was found to be intensified rapidly in strength, the separated anti-clockwise LEV on the lower surface would move downstream approaching the trailing edge of the wing. As the wing passing the neutral position during the down stroke of the flapping motion, as shown in Figs. 6b,

7b, and 8b, while the clockwise LEV formed on the upper surface was found to become much stronger, the separated anti-clockwise LEV on the lower surface was found to be pushed downstream of the wing trailing edge with the rear tip of the separated anti-clockwise LEV hanging to the trailing edge of the flapping wing. While the separated anti-clockwise LEV structure on the lower surface of the flapping was pushed to move further downstream, the clockwise LEV generated on the upper surface was found to be intensified continuously and stayed attached to the leading edge during the entire down stroke of the flapping motion. As the flapping wing reaches its bottom most position at the end of the down stroke, as revealed in Figs. 6c, 7c, and 8c, the clockwise LEV formed on the upper surface was found to be intensified significantly and cover almost entire upper surface of the wing, and ready to separate from the leading edge of the wing.

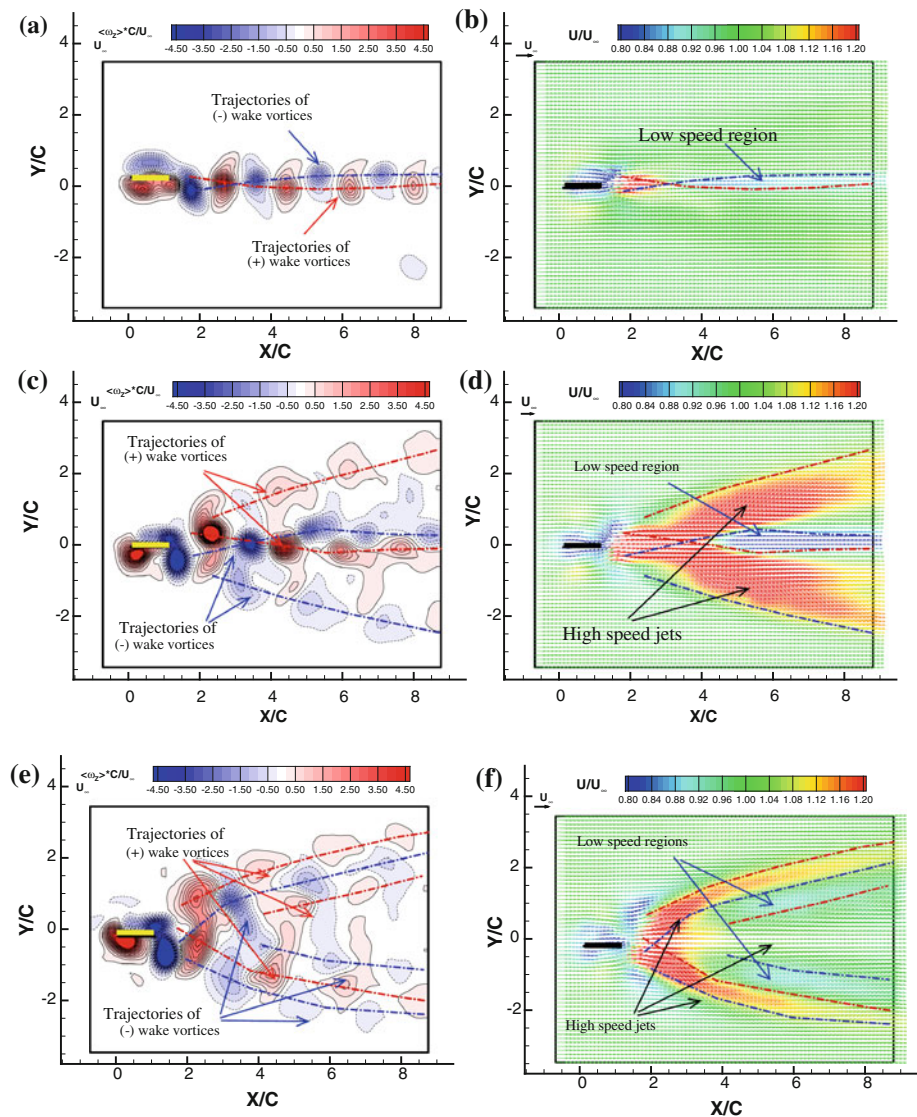
As the next upstroke starts, as shown in Figs. 6c, 7c and 8c, while the separated anti-clockwise LEV formed on the lower surface of the flapping wing from the previous upstroke would shed from the trailing edge of the flapping wing as a wake vortex, a new anti-clockwise LEV was found to form near the leading edge on the lower surface of the flapping wing. The newly formed anti-clockwise LEV on the lower surface would stay attached to the leading edge firmly while becoming stronger and stronger during the upstroke of the flapping motion. As shown in Figs. 6d, 7d, and 8d, similar as the anti-clockwise LEV on the lower

surface of the flapping wing in the course of the down stroke, the clockwise LEV on the upper surface of the flapping wing formed during the previous down stroke would separate from the leading edge and move downstream to approach the trailing edge of the flapping wing. At the end of the upstroke of the flapping circle, as shown in Figs. 6a, 7a, and 8a, the separated clockwise LEV on the upper surface would shed from the trailing edge of the wing as a wake vortex, while the newly formed anti-clockwise LEV on the lower surface would be ready to separate from the leading edge of the flapping wing. The process described earlier would repeat again and again as another down stroke and upstroke circle starts. As a result, clockwise and anti-clockwise vortex structures were found to shed alternatively in the wake of the flapping wing.

While the formation and separation scenarios of the clockwise and anti-clockwise LEV structures on the lower and upper surfaces of the flapping wing were found to be

quite similar at different wingspan locations, the evolutions of the wake vortex structures in different cross planes were found to be quite different after they shed from the trailing edge of the flapping wing. In addition to the phase-locked PIV measurement results shown in Figs. 6, 7, and 8, typical instantaneous vorticity distributions and time-averaged flowfields in the chordwise cross planes at 50, 75, and 100% wingspan (i.e., wingtip) were shown in Fig. 9 to reveal the evolution characteristics of the wake vortex structures in different cross planes downstream of the root-fixed 3-D flapping wing. The trajectories of the clockwise and anti-clockwise wake vortices were also plotted in the figures. It should be noted that the trajectories of the wake vortices were determined by tracking the centers of the spanwise vortices (i.e., at the locations where the magnitude of the spanwise vorticity reaches its local peak value) as they moved downstream based on the phase-locked PIV measurement results.

Fig. 9 Instantaneous and time-averaged PIV measurement results. **a** Instantaneous vorticity distribution at 50% wingspan. **b** Time-averaged flow field at 50% wingspan. **c** Instantaneous vorticity distribution at 75% wingspan. **d** Time-averaged flow field at 75% wingspan. **e** Instantaneous vorticity distribution at wingtip. **f** Time-averaged flow field at wingtip



As shown clearly in Fig. 6, after shedding alternatively from the trailing edge of the flapping wing, the wake structures in the cross plane at 50% wingspan were found to form concentrated vortex structures. Since the shedding of the anti-clockwise vortices would occur at the end of upstrokes, while the shedding of the clockwise vortices at the end of the down strokes, the initial positions of the anti-clockwise vortices were found to be slightly above those of the clockwise vortices. Induced by the flapping motion, the anti-clockwise vortices were found to move downward, while the clockwise vortices moved upward, as they traveled further downstream. As shown clearly in Fig. 9a, the trajectories of the clockwise and anti-clockwise wake vortices were found to cross over at the downstream location of $X/C \approx 3.0$. The concentrated wake vortices were found to align them nicely in two rows at further downstream with the clockwise vortices being slightly above the anti-clockwise vortices. According to Lai and Platzer (1999), it is a typical von Karman vortex street wake configuration for the incoming flow from left to right. Such von Karman vortex street wake configuration would cause momentum deficits in the time-averaged flow field, which was confirmed quantitatively from the time-averaged PIV measurements. As shown clearly in Fig. 9b, corresponding to the crossing over of the trajectories of the clockwise and anti-clockwise wake vortices, a long region with momentum deficits (i.e., the local flow velocity being smaller than the incoming flow velocity) was can be seen clearly at $X/C > 3.0$ downstream of the flapping wing in the cross plane at 50% wingspan. Such a wake flow pattern confirmed that the wake flow in the cross plane at 50% wingspan would be drag producing.

Compared with the cross plane at 50% wingspan, the evolution of the wake vortex structures in the cross plane at 75% wingspan was found to become much more complicated. As shown in Fig. 7, corresponding to the larger flapping amplitude at 75% wingspan, the wake vortex structures were found to be stretched in this cross plane as they shed from the trailing edge of the flapping wing. As a result, the wake vortex structures were found to have much longer “tails”, in addition to the concentrated wake vortex cores. As the same as those observed in the cross plane at 50% wingspan, since the shedding of the anti-clockwise vortices was found to occur at the end of the upstrokes, while the clockwise vortices at the end of the down strokes, the initial positions of the anti-clockwise wake vortices were found to be slightly above those of the clockwise wake vortices in the near wake region. Induced by the flapping motion of the flapping wing, the clockwise wake vortices were found to move upward, while the anti-clockwise wake vortices moving downward, as traveling further downstream. As shown clearly in Fig. 9c, the trajectories of the clockwise and anti-clockwise vortex cores

were found to cross over at the downstream location of $X/C \approx 3.5$. Right before the crossing over of the trajectories of the clockwise and anti-clockwise vortex cores, the wake vortex structures were found to break into two parts (i.e., the stretched “tails” were found to separate from the vortex cores to form additional two rows of weaker wake vortices). As a result, four rows of wake vortex structures with alternative rotation direction were found in the wake region downstream of the flapping wing at 75% wingspan. As shown clearly in Fig. 9d, corresponding to the breakdown of the vortex structures to form four rows of the wake vortices, the wake flow in the cross plane at 75% wingspan was found to split into two jet-like wake streams (i.e., bifurcation of the wake flow was observed in the wake flow at 75% wingspan). For each jet-like wake stream, a row of clockwise wake vortices were found to be above the anti-clockwise wake vortices. According to Lai and Platzer (1999), such wake vortex configuration was called reversed von Karman vortex streets for the incoming flow from left to right, which would result in momentum surfeits (i.e., thrust generation). The momentum surfeits were revealed clearly and quantitatively in the time-averaged PIV measurement result shown in Fig. 9d as the jet-like streams with local wake flow velocity much greater than the incoming flow velocity. It suggests that wake flow in this cross plane would be a thrust producing.

As shown in Fig. 8, the behavior of the wake vortex structures in the cross plane passing the wingtip was found to become much more involved due to the effects of the additional wingtip vortices in this cross plane. Instead of forming concentrated vortices as those observed in the cross planes at 50% wingspan, the wake vortex structures in this cross plane were found to be elongated significantly and broke down into smaller and weaker vortices rapidly after they shed from the trailing edge of the flapping wing. As indicated clearly in Fig. 9e, after breakdown, the smaller and weaker wake vortices were found to align themselves in six rows as they travel downstream. The smaller and weaker wake vortex structures were found to be dissipated rapidly and eventually vanished at further downstream. As shown clearly in Fig. 9f, corresponding to the formation of six rows of wake vortex structures at the downstream region of $X/C > 2.0$, the wake flow in this cross plane was found to be split into three jet-like streams with two low-speed regions filling in the gaps between the high-speed jets. It should be noted that interestingly, the high-speed jet-like wake streams were found to be in the regions where the adjacent rows of the wake vortices have the pattern of the clockwise wake vortices above the anti-clockwise vortices, i.e., typical reversed von Karman vortex street configuration. The two low-speed streams were found to be in the regions where the adjacent rows of the wake vortices have the pattern of the anti-clockwise

wake vortices above the clockwise vortices, i.e., typical von Karman vortex street configuration. Compared with those in the cross plane at 75% wingspan, the width of the wake region downstream the piezoelectric flapping wing was found to become slightly greater in the near field, and the splitting of the wake flow was also found to take place at much upstream (i.e., at $X/C \approx 2.0$ instead of $X/C \approx 3.5$).

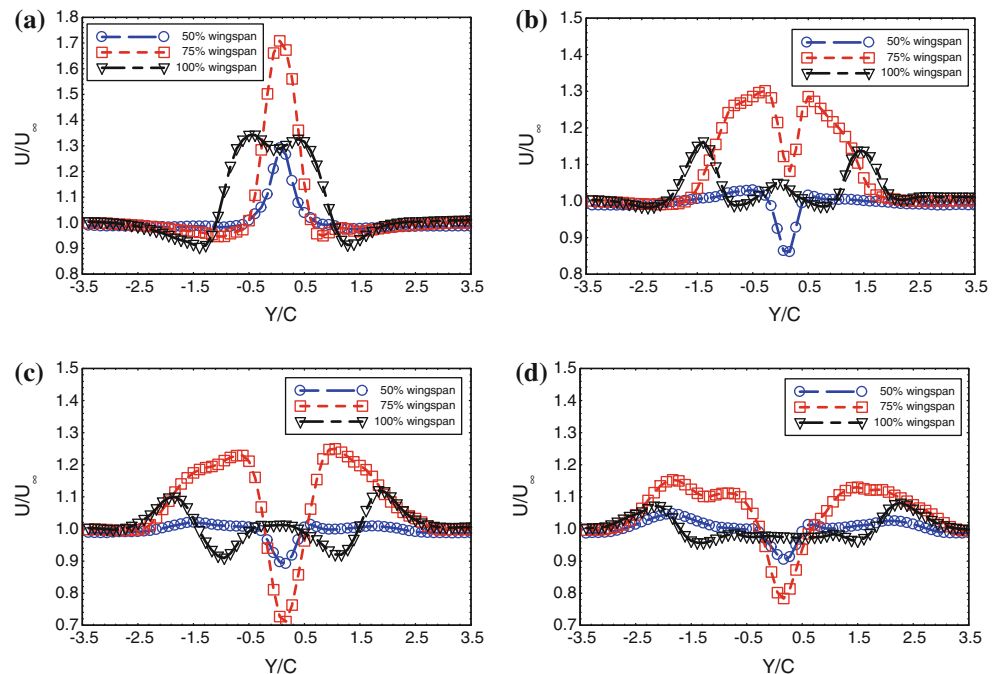
In order to reveal the characteristics of the wake flow downstream of the root-fixed 3-D flapping wing at different wingspan locations more clearly and quantitatively, the transverse profiles of the time-averaged streamwise flow velocity at downstream locations of $X/C = 2.0, 4.0, 6.0,$ and 8.0 are plotted in Fig. 10. It can be seen clearly that jet-like profiles with momentum surfeits (i.e., the local flow velocity in the wake being greater than the incoming flow) were found in the near field downstream the piezoelectric flapping wing (i.e., within one chord length downstream the trailing edge of the flapping wing) for all the three studied chordwise cross planes. As shown in Fig. 10a, the jet-like velocity profile at 75% wingspan was found to have the highest peak velocity among the three studied cross planes, while high-speed jet in the cross plane passing the wingtip was found to have the greatest width corresponding to the largest flapping amplitude at the wingtip.

The time-averaged streamwise velocity profiles in the cross plane at 50% wingspan show obvious momentum deficits (i.e., wake flow velocity being smaller than the incoming flow velocity) at further downstream locations (i.e., $X/C = 4.0, 6.0,$ and 8.0). It indicates that the wake flow in the cross plane at 50% wingspan would be drag producing, as described earlier. For the velocity profiles in

the cross planes at 75% wingspan and 100% wingspan (i.e., wingtip), since the regions with momentum surfeits (i.e., the wake flow velocity being greater than the incoming flow) were found to be much greater than those with momentum deficits (i.e., wake flow velocity being smaller than the incoming flow velocity), net momentum surfeits are expected for the wake flow in these cross planes. It confirms the thrust-producing nature of the wake flow in the cross planes at 75% wingspan and 100% wingspan (i.e., wingtip). The splitting of the wake flow into multiple jet-like streams in the cross planes passing 75 and 100% wingspan was revealed quantitatively from the time-averaged velocity profiles as the existence of multiple velocity peaks in the profiles.

In summary, the measurements in the chordwise cross planes at different wingspan locations revealed clearly that for the root-fixed 3-D flapping wing, while the inner half (i.e., the half closer to the wing root) of the flapping wing was drag producing, the outer half of the flapping wing was found to be thrust producing. It should also be noted that despite the largest flapping amplitude at wingtip, the net momentum surfeits in the cross plane at 100% wingspan (i.e., wingtip) were found to be much smaller than those in the cross plane passing the 75% wingspan. Therefore, more thrust would be expected at 75% wingspan rather than that at wingtip for the root-fixed 3-D flapping wing. The existence of the additional wingtip vortex structures is believed to be responsible for the less thrust generation at the wingtip compared with that at 75% wingspan. It should be noted that while a momentum deficit can generally be attributed to drag and a momentum surplus is associated

Fig. 10 The time-averaged streamwise velocity profiles in the wake region. **a** $X/C = 2.0$. **b** $X/C = 4.0$. **c** $X/C = 6.0$. **d** $X/C = 8.0$



with thrust, the pressure distribution in the near wake of a flapping wing/airfoil may also influence the momentum balance strongly. According to the work by Bohl and Kochesfahani (2009), the effects of the pressure distribution on the momentum balance would be reasonably small for the cases of the present study with relatively low reduced frequency of $k = 3.5$. However, the effects of the pressure distribution on the momentum balance could become significant when the reduced frequency becomes much higher.

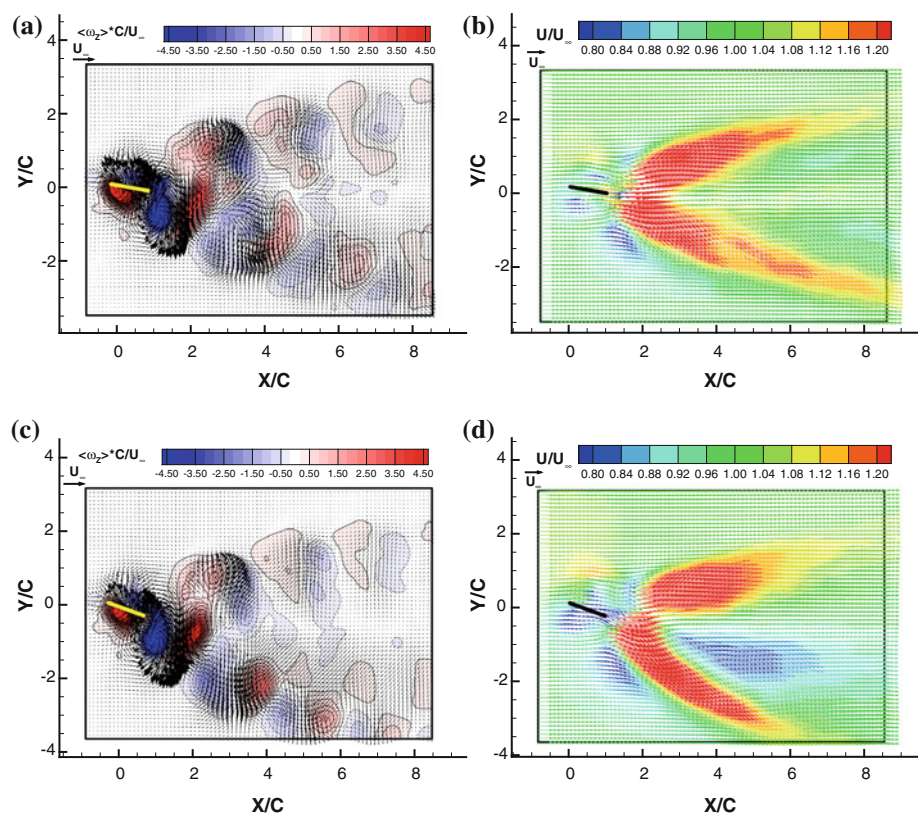
The effects of the static angle of attack (AOA) of the flapping wing on the evolution of the unsteady wake vortex structures downstream the flapping wing were also investigated in the present study. Figure 11 shows the typical instantaneous and time-averaged PIV measurement results in the cross plane passing the wingtip with the piezoelectric flapping wing having a static angle of attack of 10 deg. and 20 deg. (i.e., AOA = 10 and 20 deg), respectively. In the plots, the incoming flow velocity U_∞ was again subtracted from the measured instantaneous flow velocity vectors in order to reveal the unsteady wake vortex structures induced by the flapping motion more clearly. Similar to those revealed in the Fig. 8, alternative shedding and subsequent breakdown of the anti-clockwise and clockwise wake vortex structures can be seen clearly from the instantaneous PIV measurement results. While the wake flows with static AOA = 10 and 20 deg. were still found to split into multiple jet-like streams, they were found to become very

unsymmetrical. The downward high-speed jet stream in the lower part of the wake flow was found to be much more significant compared with the upward jet stream in the upper part of the wake flow. As a result, according to Newton's third law, a net lift force is expected to push the flapping wing upward. It indicates that the flapping wing would also be able to generate lift in addition to thrust when it is mounted with a positive static angle of attack. As shown clearly in Fig. 11, the downward high-speed jet stream in the lower part of the wake flow was found to become more and more significant as the static angle of attack increases. It indicates more and more lift would be generated with the increasing the static angle of attack of the flapping wing. Hu et al. (2010) reported similar result based on their measurements of the aerodynamic forces (both lift and thrust) generated by a flapping-wing MAV model.

4 Concluding remarks

An experimental investigation was conducted to characterize the evolution of the unsteady vortex structures in the wake of a root-fixed piezoelectric flapping wing with the wing size, stroke amplitude and flapping frequency within the range of insect characteristics. A digital particle image velocimetry (PIV) system was used to achieve

Fig. 11 The effects of the static angles of attack of the piezoelectric flapping wing. **a** Instantaneous result with static AOA = 10 deg. **b** Time-averaged result with static AOA = 10 deg. **c** Instantaneous result with static AOA = 20 deg. **d** Time-averaged result with static AOA = 20 deg



phase-locked measurement to quantify the transient behavior of the unsteady wake vortex structures in relation to the phase angles of the piezoelectric flapping wing in the flapping motion. The evolutions of the wake vortex structures in the cross planes at 50% wingspan, 75% wingspan, and 100% wingspan (i.e., wingtip) of the root-fixed 3-D flapping wings were compared quantitatively in order to elucidate underlying physics for better understanding of the unsteady aerodynamics of flapping flight for the development of novel insect-sized, flapping-wing-based nano-air-vehicles (NAVs).

The PIV measurements revealed clearly that the evolution of the wake vortices in the downstream of a root-fixed 3-D flapping wing would be much more complicated compared with those in the wakes of 2-D flapping airfoils reported in previous studies. It was found that the wake vortices in the cross plane at 50% wingspan would form concentrated vortex structures. As they travel downstream, the concentrated anti-clockwise and clockwise wake vortices were found to cross over at first and then align themselves in two rows with the clockwise (negative) vortices at above and anti-clockwise (positive) vortices below, which is a typical von Karman vortex street wake configuration for an incoming flow from left to right. Momentum deficits were confirmed in the time-averaged flow field in the cross plane at 50% wingspan, which indicates that drag, instead of thrust, would be produced at 50% wingspan of the flapping wing. The wake vortex structures in the cross planes at 75 and 100% wingspan were found to be highly stretched and break down subsequently into smaller and weaker wake vortices. After breakdown, while the wake vortex structures would align themselves in several well-organized rows as they travel downstream, the wake flow was found to be split into multiple jet-like streams. For each jet-like wake stream, the clockwise vortices were found to be above the anti-clockwise vortices, which represent a reversed von Karman vortex street configuration for the incoming flow from left to right. The measurements indicate that for the root-fixed 3-D flapping wing, while the inner half (i.e., the half of the wing close to the wing root) of the flapping wing was drag producing, the outer half of the flapping wing was found to be thrust producing. Majority of the thrust was found to be generated in the neighborhood of 75% wingspan instead of the region near wingtip due to the detrimental effects of the wingtip vortices. In addition to thrust generation, the flapping wing would also be lift producing when it is mounted with a positive static angle of attack.

While the 2-D PIV measurement results (i.e., both phased-locked and ensemble-averaged PIV results) given in the present study elucidated clearly and quantitatively that the characteristics of the wake flow at the downstream of a root-fixed 3-D flapping wing would be significant

different from those in the wakes of 2-D flapping airfoils reported in previous studies, providing additional spanwise component of the flow velocity field would be very helpful to reveal the 3-D features of the complex vortex and flow structures in the wake of the root-fixed 3-D flapping wing more clearly. It is planned to conduct stereoscopic PIV measurements to quantify the complex wake vortex and flow structures at the downstream of a root-fixed 3-D flapping wing in the future as an extension of the present study.

Acknowledgments The authors also want to thank Mr. Bill Rickard of Iowa State University for his help in conducting the wind tunnel experiments. The support of National Science Foundation CAREER program under award number of CTS-0545918 is gratefully acknowledged.

References

- Anderson JM, Streitlien K, Barrett DS, Triantafyllou MS (1998) Oscillating foils of high propulsive efficiency. *J Fluid Mech* 360:41–72
- Bohl DG, Koochesfahani MM (2009) MTV measurements of the vortical field in the wake of an airfoil oscillating at high reduced frequency. *J Fluid Mech* 620:63–88
- Bohorquez F, Samuel P, Sirohi J, Pines D, Rudd L, Perel R (2003) Design analysis and hover performance of a rotating wing Micro Air Vehicle. *J Am Helicopter Soc* 48(2):80–90
- Chung HC, Kummari KL, Croucher SJ, Lawson NJ, Guo S, Whatmore RW, Huang Z (2009) Development of piezoelectric fans for flapping wing application. *Sens Actuator A* 149:136–142
- Clemons L (2009) An experimental study of the vortex structures in the wake of a piezoelectric flapping plate for Nano Air Vehicle applications. MS thesis. Department of Aerospace Engineering of Iowa State University
- Cox A, Monopoli D, Cveticanin D, Goldfarb M, Garcia E (2002) The development of elastodynamic components for piezoelectrically actuated flapping micro air vehicles. *J Intell Mater Syst Struct* 13:611–615
- Dickinson MH, Lehmann FO, Sane SP (1999) Wing rotation and the aerodynamic basis of insect flight. *Science* 284:1954–1960
- Freythuth P (1988) Propulsive vortical signatures of plunging and pitching airfoils. *AIAA J* 26(7):881–883
- Garrick IE (1936) Propulsion of a flapping and oscillating airfoil. NACA Report. 567, May 1936
- Hu H, Gopa-Kumar A, Abate G, Albertani R (2010) An Experimental study of flexible membrane wings in flapping flight. *Aerosp Sci Technol* 14(8):575–586
- Jones KD, Dohring CM, Platzer MF (1996) Wake structures behind plunging airfoils: a comparison of numerical and experimental results. 34th Aerospace sciences meeting and exhibit, Reno, NV, AIAA Paper 96-0078, 1996
- Koochesfahani MM (1989) Vortical patterns in the wake of an oscillating airfoil. *AIAA J* 27(9):1200–1205
- Lai JCS, Platzer MF (1999) Jet characteristics of a plunging airfoil. *AIAA J* 37(12):1529–1537
- Lewin GC, Haj-Hariri H (2003) Modelling thrust generation of a two-dimensional heaving airfoil in viscous flow. *J Fluid Mech* 492:339–362
- Maxworthy T (1981) The fluid dynamics of insect flight. *Ann Rev Fluid Mech* 13:329–350

- Mueller TJ (2001) Fixed and flapping wing aerodynamics for Micro Air Vehicle applications (Progress in Astronautics and Aeronautics), ISBN 1-56347-517-0
- Niezrecki C, Brei D, Balakrishnan S, Moskalik A (2001) Piezoelectric actuation: state of the art. *Shock Vib Dig* 33:269–280
- Park HC, Kim KJ, Lee S, Lee SY, Cha YJ, Yoon KJ, Goo NS (2004) Biomimetic flapping devices powered by artificial muscle actuators. Proceedings of UKC2004 US–Korea Conference on Science, Technology and Entrepreneurship, August, 2004
- Ramasamy M, Leishman JG, Lee TE (2006) Flow field of a rotating wing MAV. 62nd Annual National Forum Proceedings of the American Helicopter Society
- Read DA, Hover FS, Triantafyllou MS (2003) Forces on oscillating foils for propulsion and maneuvering. *J Fluid Struct* 17:163–183
- Sunada S, Ellington CP (2001) A new method for explaining the generation of aerodynamic forces in flapping flight. *Math Methods Appl Sci* 24:1377–1386
- Taylor GK, Nudds RL, Thomas ALR (2003) Flying and swimming animals cruise at a Strouhal number tuned for high power efficiency. *Nature (London)* 425:707–711. doi:[10.1038/nature02000](https://doi.org/10.1038/nature02000)
- Toda M (1981) Voltage-induced large amplitude bending device—PVF2 bimorph—its properties and applications. *Ferroelectrics* 32:911
- Triantafyllou MS, Triantafyllou GS, Gopalkrishnan R (1991) Wake mechanics for thrust generation in oscillating foils. *Phys Fluids A* 3:2835–2837
- Triantafyllou GS, Triantafyllou MS, Grosenbaugh MA (1993) Optimal thrust development in oscillating foils with application to fish propulsion. *J Fluids Struct* 7:205–224
- Wang ZJ (2000) Vortex shedding and frequency selection in flapping flight. *J Fluid Mech* 410:323–341
- Wood RJ (2008) The first takeoff of a biologically-inspired at-scale robotic insect. *IEEE Trans Robotics* 24(2):341–347
- Wu PR, Kingon A, Mulling J (2003) Piezoelectric resonating structures for microelectronic cooling. *Smart Mater Struct* 12:181–187
- Yoo JH, Hong JI, Cao W (2000) Piezoelectric ceramic bimorph coupled to thin metal plate as cooling fan for electronic devices. *Sens Actuator A* 79:8–12
- Young J, Lai JCS (2004) Oscillation frequency and amplitude effects on the wake of a plunging airfoil. *AIAA J* 42(10):2042–2052
- Youngren H, Kroninger C, Chang M, Jameson S (2008) Low Reynolds number testing of the AG38 airfoil for the SAMARA nano air vehicle. AIAA 2008-417, 46th AIAA Aerospace Sciences Meeting and Exhibit, 7–10 January 2008, Reno, Nevada